




Investigations of electrical properties of $\text{Pr}_{0.65}\text{Ca}_{0.25}\text{Cd}_{0.1}\text{MnO}_3$ ceramic

A. Khlifi¹, R. Hanen¹, A. Mleiki^{1,2,a} , H. Rahmouni¹, N. Guerhazi³, K. Khirouni⁴, A. Cheikhrouhou²

¹ Unité de recherche Matériaux Avancés et Nanotechnologies (URMAN), Institut Supérieur des Sciences Appliquées et de Technologie de Kasserine, Kairouan University, BP 471, 1200 Kasserine, Tunisia

² LT2S, Digital Research Center of Sfax, Sfax Technoparc, 3021 Sfax, Tunisia

³ Laboratoire de Génie des Matériaux et Environnement (LGME), Ecole Nationale d'Ingénieurs de Sfax (ENFS), BP 1173-3038, Sfax, Tunisia

⁴ Laboratoire de Physique des Matériaux et des Nanomatériaux Appliquée à l'Environnement, Faculté des Sciences de Gabès cité Erriadh, Université de Gabès, 6079 Gabès, Tunisia

Received: 8 August 2020 / Accepted: 22 September 2020 / Published online: 7 October 2020
© Società Italiana di Fisica and Springer-Verlag GmbH Germany, part of Springer Nature 2020

Abstract $\text{Pr}_{0.65}\text{Ca}_{0.25}\text{Cd}_{0.1}\text{MnO}_3$ ceramic was elaborated using the conventional solid-state reaction technique. The polycrystalline sample was subjected to investigate by ac impedance spectroscopy. From the main results, the electrical conductivity analysis confirms the semiconductor behavior and indicates that the hopping process governs the electrical conductivity. From ac-conductivity, two distinct mechanisms are observed. Indeed, the conduction mechanism is attributed to the correlated barrier hopping model in the middle of the frequency region and the overlapping large polaron tunneling in the high-frequency one. The analyzed impedance and modulus confirmed the presence of non-Debye-type relaxation phenomenon. Different electrical equivalent circuits were used to analyze the Nyquist plots. The obtained results confirm the contribution of grain boundary on the conduction. The increase in dielectric constant and the rate of its increase at low frequency were related to the disorder of the cation sublattices.

1 Introduction

For many decades, solid oxide fuel cells (SOFCs) have attracted much attention, as a new electric power source, due to the efficiency of high energy conversion and the absence of air pollution emission. The electrolytes and electrodes are the essential components of the SOFC. However, the performance of this later remains dependent on the electrical conductivity and the overpotential of the cathode–electrolytes interface as reported in Ref [1]. In addition, the electrical conductivity and cathodic overpotentials are very sensitive to the rare earth cations used for the A-sites of perovskite oxide [2–6]. In this context, manganite materials have been studied and widely used as a cathode for SOFC [7]. In addition, these materials have essential utilization in numerous applications such as magnetic sensors, computer memory systems, and magnetic refrigerants [8–10]. The Pr-based manganite is one of the important members in the manganite family due to their variety of phases, multifunctional properties, and their

^a e-mail: alimlk1986@hotmail.com (corresponding author)

rich fundamental physics. The parent compound PrMnO_3 shows a transition from insulating paramagnetic to an insulating A-type antiferromagnetic at $T_N = 99$ K [11]. Also, the destabilization/destruction of charge ordering state leads to very interesting structural, electrical, and magnetic properties [7]. Moreover, doping PrMnO_3 by a divalent element such as Ca [12, 13], Sr [13, 14], and Ba [15, 16] was studied by various research groups. In particular, the doping of divalent Ca^{2+} at the Pr-site shows fascinating properties that depend on the interplay of charge, orbital, lattice, and spin ordering [17]. The maintain of the charge balance leads to the decrease in Mn^{3+} at the cost of Mn^{4+} ions when the Ca^{2+} replacing Pr^{3+} ions in the parent compound PrMnO_3 . Furthermore, the praseodymium-calcium manganite shows many novel properties such as ferroelectricity, charge ordering (CO), and ferromagnetism. By applying a large magnetic field ($H = 6$ T), the electrical resistivity of the oxide $\text{Pr}_{0.65}\text{Ca}_{0.35}\text{MnO}_3$ decreases six orders of magnitude. This compound is characterized by the presence of charge ordering (CO) state at $T = 225$ K and the appearance of paramagnetic-ferromagnetic state transition at low temperatures. Also, its electrical conduction shows an insulator behavior [18]. On the other hand, cadmium oxide has potential applications in optoelectronic and catalytic such as phototransistors [19], photodiodes [20], solar cells [21, 22], electrodes, and gas sensors [23]. Under temperature and magnetic field, this compound is identified by its chemical stability and its non-toxicity. Gupta et al. [24] have reported that this later has a low electric resistivity, high transmission in the visible region, and a semiconductor property with a large bandgap. Moreover, the ionic radii of Ca and Cd are close to 0.134 and 0.131 nm, respectively. Then, doping with Cd leads to interesting results as obtained as Ca doping [25]. Such supposition was confirmed by Araùjo et al. [26]. In fact, the colossal magnetoresistance with ferromagnetic behavior and the value of Curie temperature ($T_c \approx 250$ K) for $\text{La}_{0.67}\text{Cd}_{0.33}\text{MnO}_3$ are the same for Ca doping with the same level. Additionally, many reports [27–30] have shown that the doping with Cd ions leads to the depression of the metallic state and gives rise to the insulator behavior. According to the literature, such behavior was explained by the stability of the impurity centers of $\text{Cd}^{2+}\text{-Mn}^{4+}$ [27], and the strong DE interaction with moderate Jahn–Teller distortions [31]. Pena et al. [32] have considered that the substitution of Ca^{2+} by Cd^{2+} on $\text{La}_{0.7}(\text{Ca}_{0.3-x}\text{Cd}_x)\text{MnO}_3$ ($0 \leq x \leq 0.3$) suppressed the double exchange mechanism which weakness both ferromagnetic and metallic characters. As the Cd content increases, the metallic-semiconductor behavior decreases and the insulator character dominates in the whole temperature range for $x = 0.3$.

The major goal of the investigations presented in this work is to study the physical properties of $\text{Pr}_{0.65}\text{Ca}_{0.25}\text{Cd}_{0.1}\text{MnO}_3$ ceramic prepared by the conventional solid-state reaction method.

2 Experimental details

A powder sample of $\text{Pr}_{0.65}\text{Ca}_{0.25}\text{Cd}_{0.1}\text{MnO}_3$ is prepared using the conventional solid-state reaction method. Stoichiometric quantities of precursors Pr_6O_{11} , CaCO_3 , CdCO_3 , and MnO_2 , with high purity 99.99%, are used. The basis to an agate mortar, the proportions of powder are mixed and then treated by high temperature according to the following reaction:



The obtained powder was calcinated at 900 °C for 12 h, compacted into pellet form under a uniaxial pressure of 5 tons, and sintered at 1000 °C for 24 h. At last, the sample was annealed at 1200 °C for 24 h. The crystalline structure and the purity of the phase are examined at room temperature using X-ray powder diffraction with $\text{Cu-K}\alpha$ radiation ($\lambda = 1.5406$ Å). The

structure refinement was carried out by the Rietveld analysis integrated into FULLPROF software. The Rietveld refinement of the XRD measurement suggests the sample belongs to *Pnma* space group. The structural parameters of the unit cell are $a = 5.4471 \text{ \AA}$, $b = 7.6761 \text{ \AA}$ and $c = 5.4245 \text{ \AA}$.

To conduct electrical measurements, and based on the thermal evaporation, a thin silver film was deposited on both sides of the pellet. Then, the configuration of the plate capacitor was obtained and it is used to measure the conductance and the capacitance. In order to vary the temperature from 80 to 300 K, the sample is mounted in a cryostat. Then, we used an Agilent 4294A analyzer to measure the conductance and the capacitance at different temperatures and frequencies.

3 Results and discussion

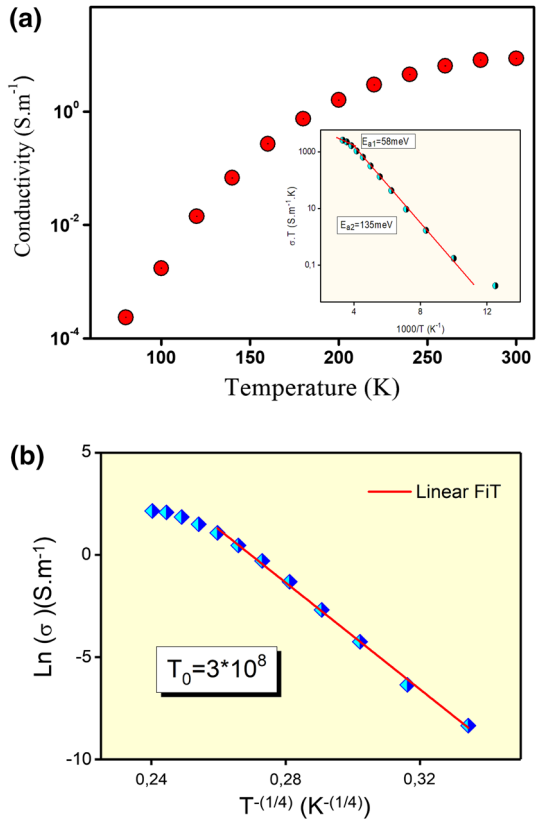
3.1 Dc-conductivity analysis

Figure 1a shows the variation of dc-conductivity as a function of temperature. The increase in σ_{dc} with the temperature indicates that the investigated ceramic exhibits a semiconductor behavior. At higher temperatures, a saturation region seems to appear at around room temperature. Many researchers [33–35] reported that several parameters are responsible for the appearance of the saturation region. When the temperature increases, the carriers acquire sufficient thermal energy to cross easily the encountered barriers. Therefore, the density of free carriers rises. Moreover, the reduction of the efficient capture of charge traps suggesting the vanishing of the available density of trapped charge. It is also noted that the substitution on Ca ion by Cd increases the conductivity as compared to the parent compound [18]. In order to get information about the type of conduction mechanism present in $\text{Pr}_{0.65}\text{Ca}_{0.25}\text{Cd}_{0.1}\text{MnO}_3$, we used two hopping models [36]. At high temperatures, the experimental data are well fitted using the small polaron hopping (SPH) model (inset of Fig. 1a). Such a model is described mathematically by the relation $\sigma T = \sigma_0 \exp(E_a/k_B T)$, where σ_0 is a pre-exponential factor, E_a is the activation energy, k_B is the Boltzmann constant and T is the absolute temperature. At low temperatures, the variable range hopping (VRH) model is the used model to fit the experimental data (see Fig. 1b). Such model is defined by $\sigma = A \exp(-T_0/T)^{1/4}$, where T_0 is the temperature factor and described by $T_0 = 16\alpha^3/k_B \cdot N(E_F)$. The value of such constant occurs $3 \times 10^8 \text{ K}$ and it is in good agreement with other results [37]. In the low-temperature range, the existence of localization centers of trapped charge with various activation energies values controlled the transport of carriers. When the temperature increases, such centers released carriers, and the SPH mechanism governed the conduction. The deduced activation energy is $E_{a1} = 58 \text{ meV}$ and $E_{a2} = 135 \text{ meV}$, in the temperature range of 80–240 K and 240–300 K, respectively.

3.2 Ac-conductivity analysis

The temperature evolution of ac-conductivity (σ_{ac}) as a function of frequency is shown in Fig. 2. Such variation indicates that the investigated sample exhibit a semiconductor behavior in the whole temperature range and for a different frequency. Especially, at high frequency, a saturation region seems to appear at around $T_{\text{sat}} = 200 \text{ K}$. The increase in conductivity with increasing temperature and frequency can be related to the rise of hopping frequency and drift mobility of the charge carrier [38]. The same behavior has been observed in several oxides and amorphous materials [33, 39]. Moreover, Pike model [39] is the used one to

Fig. 1 **a** Temperature dependence of conductivity for $\text{Pr}_{0.65}\text{Ca}_{0.25}\text{Cd}_{0.1}\text{MnO}_3$ ceramic. The inset shows the variation of (σT) versus $(1000/T)$, **b** variation of (σ) versus $(T^{-1/4})$

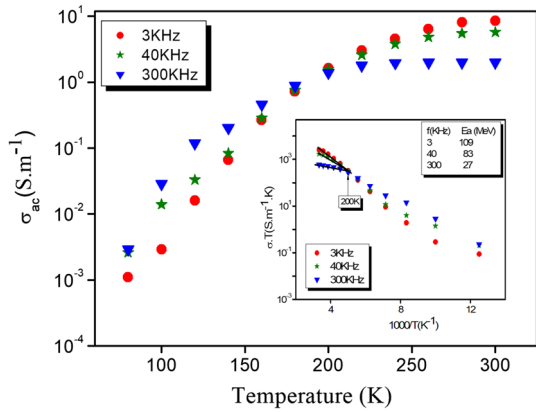


analyze such behavior. Indeed, the ac hopping conduction of the localized carriers can be the origin of the evolution of ac-conductivity with both frequency and temperature. Additionally, at a specific temperature value, the conductivity is frequency independent. It is also clearly seen that at high temperatures and with increasing frequency the conductivity decreases, indicating the metallic behavior. At high temperatures, the larger amplitude of vibration and the polaron scattering lead to the rise of the resistivity, which explained the appearance of metallic behavior. The inset of Fig. 2. displays the variation of $\sigma_{ac}T$ versus $1000/T$ at selected frequencies. The activation energy (E_{ac}) values are deduced using:

$$\sigma_{ac}T = B \exp\left(\frac{E_{ac}}{k_B T}\right) \tag{1}$$

It is found that the activation energy values decrease with increasing frequency confirming the change in electrical behavior of the compound from semiconductor to metallic one. Furthermore, the activation energy values deduced from ac-conductivity are lower than those deduced from dc-conductivity. In some cases, the hopping mechanism includes sites with a large distance between ions. When the frequency increases, the hopping of charge carriers was realized only between the neighbor sites. This, explain the decrease in activation energy values with increasing frequency. Rahmouni et al. [40] have been reported that the accessibility of other sites in ac-conductivity can be the origin of the lowest values of activation energy involved in ac-conductivity than those of dc-conductivity. The plot of σ_{ac} versus frequency

Fig. 2 Temperature dependence of electrical conductivity at selected frequencies. The inset presents the evolution of $\ln(\sigma_{ac}T)$ versus $(1000/T)$



in three temperature ranges is presented in Fig. 3a–c. In the first range [80–120 K], the increase in ac-conductivity with frequency reveals the existence of two slopes. Therefore, a two frequency exponent of such variation is evident. So, the simple Jonscher power law [41, 42] is modified as a double Jonscher power law response. According to Funke [43], this later follows the jump relaxation model (JRM) and is developed by Elliot [44]. So, the double power law can be described by the following equation:

$$\sigma_{ac} = \sigma_{dc} + A\omega^{s_1} + A\omega^{s_2} \tag{2}$$

where the exponent s_1 ranges from $(0 \leq s_1 \leq 1)$ characterizes the low-frequency region and it indicates the short-range translational ion hopping (non-diffusing mode). For the high frequency range, the exponents $(0 \leq s_2 \leq 2)$ corresponds to the localized relaxation/reorientational process [45]. Satapathy et al. [46] explained the appearance of two dispersion curves on ac-conductivity versus frequency to the prominent contribution of grain and grain boundary to the electrical process in the material. In the temperature region [140–180 K], the conductivity spectrum is characterized by the presence of frequency-independent region followed by a dispersive behavior at high frequency. In such temperature range, the ac-conductivity can be described by the simple Jonscher’s power law [41, 42]:

$$\sigma_{ac} = \sigma_{dc} + A\omega^{s_1} \tag{3}$$

For the third temperature range [200–300 K] and at high frequency, the $\text{Pr}_{0.65}\text{Ca}_{0.25}\text{Cd}_{0.1}\text{MnO}_3$ exhibits a metallic behavior. At higher frequencies, the hopping mechanism is weak and the conductivity was controlled by the collisions. The ac response is well described by the Drude model [47]:

$$\sigma_{ac} = \frac{\sigma_{dc}}{1 + \omega^2 \tau_s^2} \tag{4}$$

where τ_s is the relaxation time which describes the electron–phonon scattering.

In order to identify the processes contributing to the conduction mechanism, the temperature dependence of the exponent s_1 and s_2 with temperature is plotted in Fig. 3d, e. The exponent s_1 decreases with temperature until it reaches a minima value then it increases. This variation proves that the overlapping large polaron tunneling (OLPT) is the appropriate model describing the conduction mechanism. This mechanism is characterized by the overlapping of the spatial extension of large polaron with each other. This large polaron in the grain interior region is formed as a result of the coupling of doublet $\text{Mn}^{3+} \rightarrow \text{Mn}^{4+}$ and

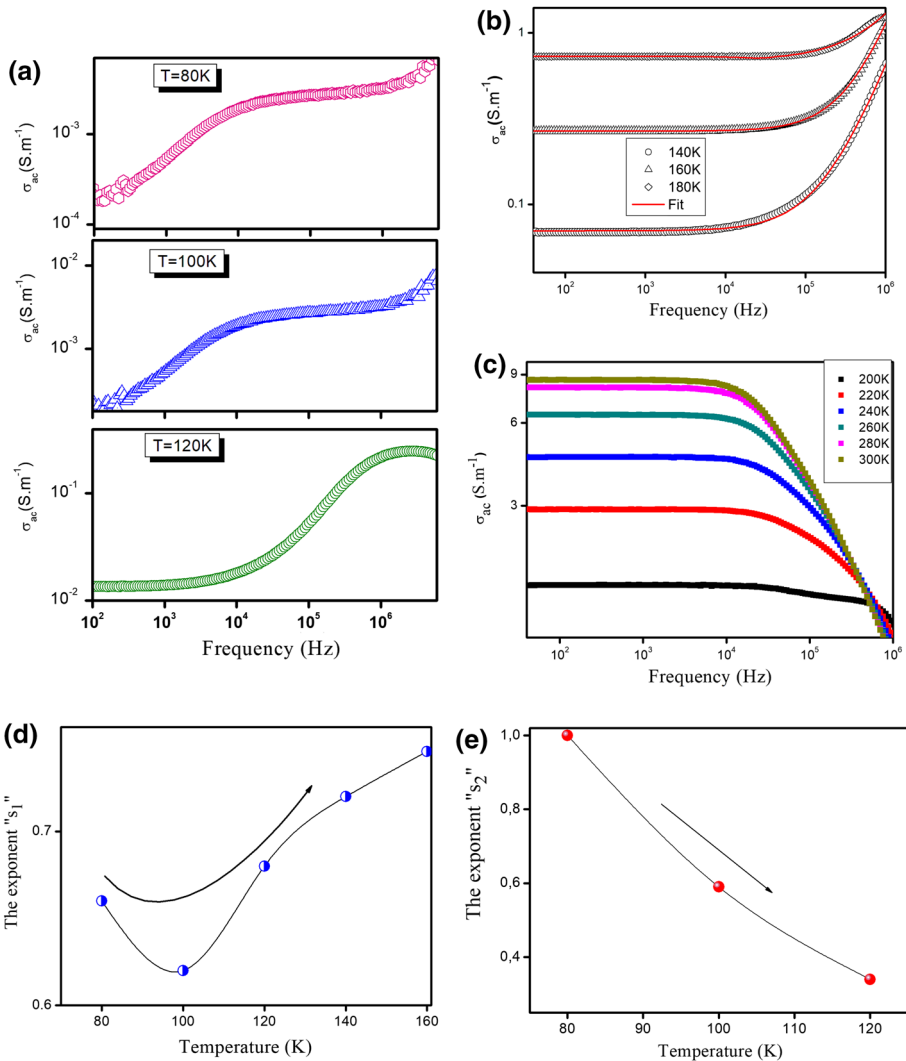


Fig. 3 Evolution of conductivity as function of frequency at different temperature ranges [80–120 K] (a), [140–180 K] (b) and [200–300 K] (c). **d, e** Variation of the exponent “ s_1 ” and “ s_2 ” as a function of temperature

lattice distortion. Therefore, a potential well around Mn⁴⁺ ions was created. Consequently, the hopping of the electron Mn³⁺ in those wells and the trapped charge carriers at the localized sites may be transformed into large polaron [48–50].

The exponent s_2 obtained from the high-frequency range decreases as the temperature increases. So, the conduction mechanism is described by the correlated barrier hopping (CBH). The hopping of small polaron or bipolaron over the Coulomb barrier which isolated two defect centers is the origin of the conduction in this mechanism. Indeed, the Jahn–Teller electron phonon-cooperation of Mn³⁺ ions is the source of the existence of small polaron, and the increase in the number of charge carriers with the rise of temperature may be the origin of bipolaron formation [51]. It may be possible that the substitution of Ca ion with Cd

generated structural and chemical defects that play the roles of defect centers. As found in the literature [48, 49, 52], the grain boundary acts as the potential barrier, isolating the defect centers due to its higher resistivity.

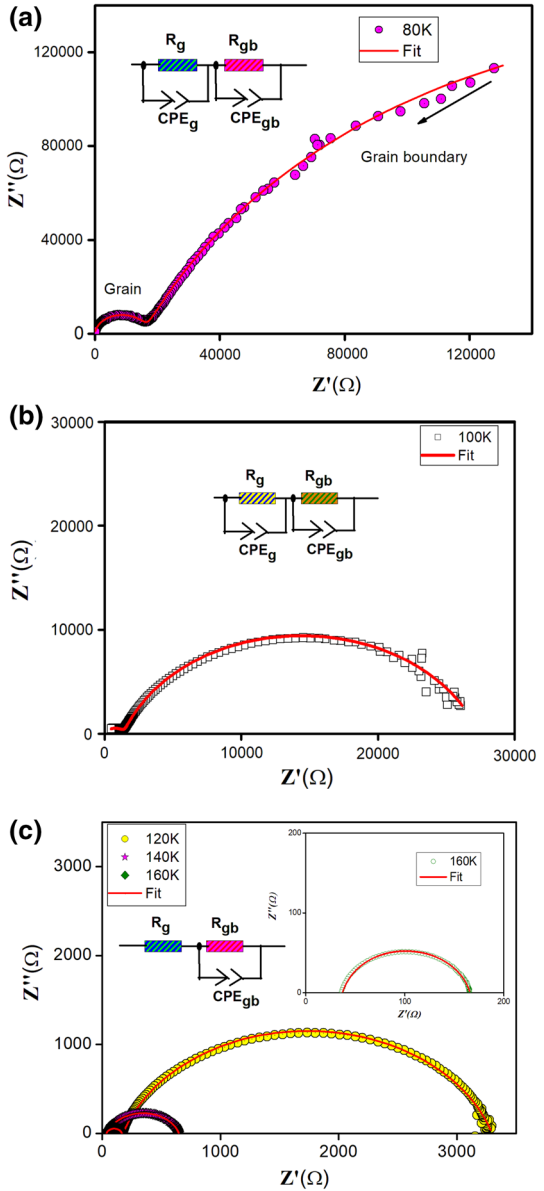
3.3 Impedance spectroscopy analysis

The variation of imaginary part Z'' as a function of real part Z' (i.e., Nyquist diagram) measured at different temperatures is depicted in Fig. 4a–c. It is clearly shown that the shape of semicircle arcs changes with increasing temperature. For $T = 80$ K and at low frequency, the high-capacitive behavior with high values of resistance is the characteristic of the grain boundary region. Moreover, the semicircular arc at high frequency, which identifies the response of grain, presents a relatively low value of both capacitance and resistance. The same behavior was observed by Khobkar et al. [53]. For $T = 100$ K, two arcs are observed. The different electrically active regions are the origins of the appearance of the two semicircle arcs [54]. The center of the semicircular arc is localized below the real axis reflecting a non-Debye-type relaxation process [55]. Generally, the grain region is characterized by a smaller relaxation time than that for the grain boundary. Therefore, the small arc in the Nyquist plot at high frequency corresponds to the contribution of grain, while the larger low-frequency arc is detected to the grain boundary one [56]. However, beyond $T = 100$ K, the larger arc at low frequencies becomes dominant and the smaller one is obscured. Therefore, a single arc is detected. Condo et al. [54] have explained the disappearance of small grain response at high temperatures by the large difference in the magnitudes of resistance between grain and grain boundary. It is also clearly seen that the diameters of the semicircular arcs decrease with increasing temperature. Such a result confirms the thermal activation of conduction processes and confirms the semiconducting behavior of the sample.

In order to correlate the electrical properties and microstructure of materials, electrical equivalent circuit models are used via ZView software (inset Fig. 4.). For $T = 80$ and 100 K, it is observed that the introduction of constant phase element (CPE) in the equivalent circuit with the effect of grain, grain boundary allows the best fit of the impedance plot. For $T > 100$ K, the equivalent circuit model is composed by $[R_g + (R_{gb}/CPE_{gb})]$. The impedance of the constant phase element is $Z_{CPE} = A^{-1}(j\omega)^{-\alpha}$ [57]. For $A = C$ and $\alpha = 1$, the CPE described the ideal capacitor. For $\alpha < 1$, Bhomik et al. [58] have shown that CPE suggests the non-Debye-type dielectric relaxation. Such behavior implies a distribution of R–C networks and heterogeneities in the material [58].

Figure 5a shows the normalized imaginary part of impedance (Z''/Z''_{\max}) as a function of frequency at different temperatures. The curves show that Z'' increases until it reaches maxima peak, above which, it decreases indicating the presence of relaxation phenomenon. Asoudi et al. [59] have reported that the presence of an asymmetric peak which describes the distribution of relaxation time can be related to the distortion of Mn–O–Mn angle bond and Jhan–Teller effect. Also, the asymmetric broadening at higher frequency confirms the contribution of grains and grain boundary in the material impedance. The accumulation of space charges and their release at lower and higher frequencies, respectively, induce the merging of curves at higher frequency [60, 61]. Furthermore, the relaxation frequency peak (f_{\max}) shifts to a higher frequency range when the temperature increases. This behavior suggests the increase in carrier mobility. The values of f_{\max} are extracted from the position of those peaks and hence the relaxation time (τ) is deduced using the relation: $\tau_0 = 1/2\pi f_{\max}$.

Fig. 4 Complex impedance spectra at different temperatures. Inset: the appropriate equivalent electrical circuit



The Arrhenius function can describe the dynamics of the relaxation process following the relation:

$$\tau = \tau_0 \exp\left(\frac{E_a}{k_B T}\right) \tag{5}$$

where τ_0 is the pre-exponential factor, k_B is Boltzmann's constant, and E_a is the activation energy.

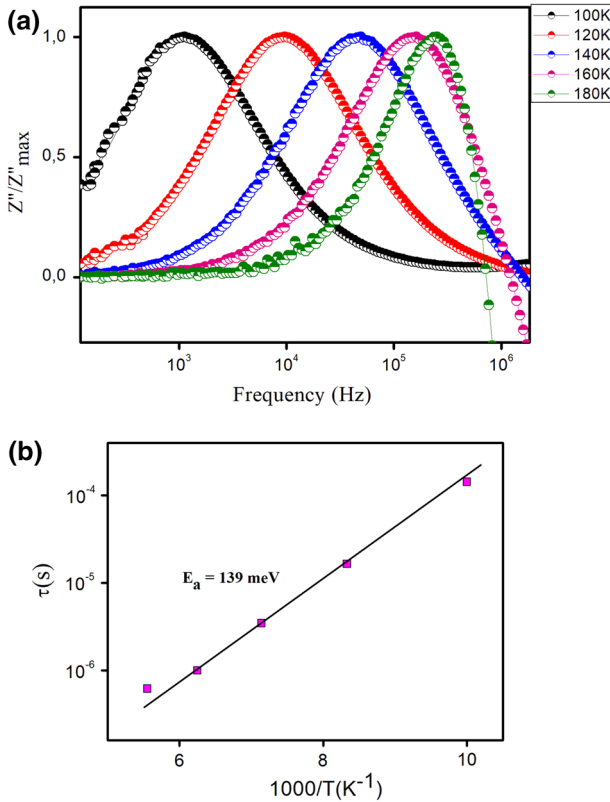


Fig. 5 The frequency dependence of Z''/Z''_{max} at different temperatures. **b** Variation of (τ) versus $1000/T$

The variation of $\ln(\tau)$ versus $1000/T$ is shown in Fig. 5b. From the slope of the linear fit, we deduce the activation energy value ($E_{a\tau}$). Such value is equal to 139 meV and it is in good agreement with E_{a2} obtained from dc-conductivity. The difference between these two activation energies is small. Indeed, the conduction mechanism involves three types of energy: hopping energy, disorder energy, and the binding one, while the relaxation process involves only the hopping energy of carriers between the localized states [62, 63]. The obtained results confirm the contribution of grain boundary on the conduction.

The variation of Z'' and M'' as a function of frequency is depicted in Fig. 6a, b at 80 and 100 K, respectively. As found in the literature, the impedance plot gives insight into the more resistive part while modulus presents the least capacitive one [64]. Moreover, Hassen et al. [45] have reported that such combined plots enable to differentiate between the short-range (i.e., localized dielectric relaxation) and the long-range (i.e., non-localized: long-range conductivity). Generally, the impedance and dielectric modulus follow $\tau_Z \geq \tau_M$ [65]. This general order explained the appearance of Z'' maximum peak at a lower frequency compared to that of M'' . The separation between these peaks suggests that the relaxation process is dominated by localized hopping of charge carriers [66, 67]. For $T = 80$ K, the curves show a single peak and it appears at the same frequency value. Such a result represents the domination of long-rang movement of charge carriers [66]. For $T = 100$ K, it is clearly seen that the gap

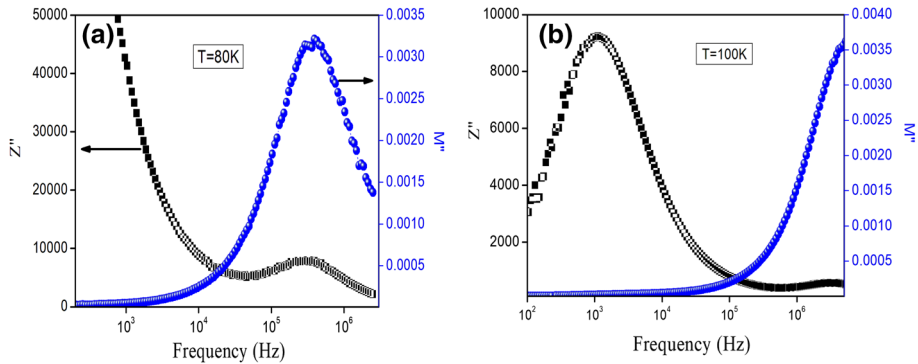


Fig. 6 Combined plots imaginary part of impedance Z'' and imaginary part of modulus M'' versus frequency at 80 K (a) and 100 K (b)

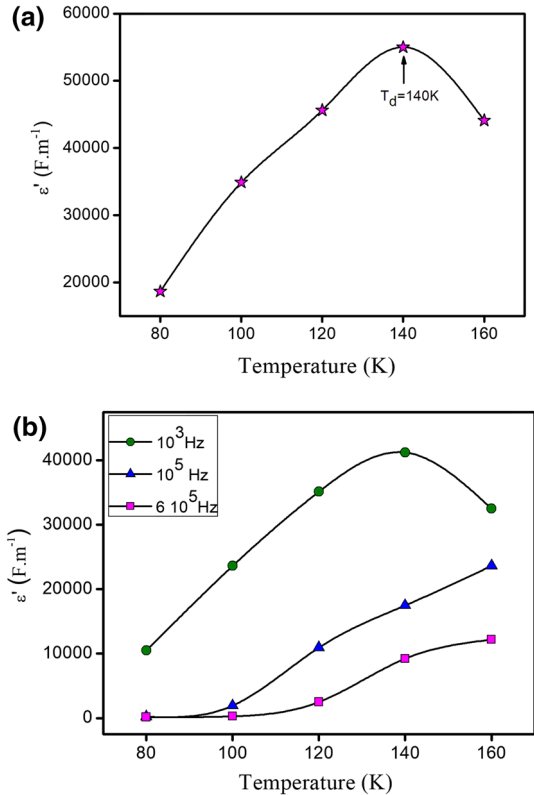
between the peak of Z'' and M'' is wide which announces the Non-Debye-type relaxation behavior [68].

3.4 Dielectric properties

The study of dielectric responses with frequency and temperature gives information about the electrical behavior of the compound. The response of the sample to an applied electric field can be related to the contribution of different types of polarization [69]. Figure 7a shows the temperature dependence of dielectric constant. The dielectric constant (ϵ') increases with temperature up to the specific temperature. This later is defined as the dielectric transition temperature T_d . Nevertheless, beyond this temperature, ϵ' value decreases. The change in the evolution of the dielectric constant with temperature can be related to the existence of a magnetic transition. Mohan et al. [70] have found a good agreement between the dielectric transition and the magnetic one and indicate the becoming of the material to paramagnetic behavior.

Figure 7b displays the variation of ϵ' with the temperature at different frequencies. The values of ϵ' increase with decreasing frequency. Such evolution characterized the compound with normal behavior (i.e., having mobile carriers) [71]. In the beginning, ϵ' starts to increase with increasing temperature. Indeed, the increase in temperature leads to the rise of polarization producing the thermal energy to the material [72]. Also, it can be observed that the rate of increase ϵ' at 10^3 Hz is the most faster than the other values of frequency. As found in the literature [73, 74], this behavior can be related to the disordering of the cation sublattices. This disorder is defined by the shift of cation from the site of the interstices to another. Indeed, this later facilitates substantially the formation of the carriers. The accompanying of the disorder of lattice with the increase in ϵ' induces the weakness of the Coulomb interaction between the departed cation and the vacancy which left it. Additionally, the transition of cations from sites to interstices leads to the production of an equivalent dipole with a positive charge in the interstice and the negative one in the site. With the applied electrical field, such dipole was oriented, and then an increase in dipole moment of the system was achieved. The increase of departure of cation from interstices induces an increase in polarizability of the unit cell. Although a discount between the interactions of an equivalent dipole, the statistical causes should be the reason for the increase in the number of such dipoles with temperature. Therefore, with increasing temperature, an occur of transition from an ordered cation sublattice

Fig. 7 **a** Temperature dependence of the real part ϵ' of the permittivity, **b** temperature dependence of ϵ' at different frequencies



(i.e., state of low ϵ') into a disordered one (i.e., state of high ϵ'). Kar [75] announces that the high value of ϵ' leads to the rise of charge carriers that are responsible for the increase in conductivity of the compound, as explained above. However, the appearance of a peak at a specific temperature (T_d) was distinguished. It is observed that with increasing frequency the value of T_d shifts to the higher temperature side indicating the presence of dielectric relaxation in the material. Rai et al. [76] explain this behavior by the increase in kinetic energy of hopping polarons, which induces the begging of oscillation of $\text{Mn}^{3+}/\text{Mn}^{4+}$ dipoles with increasing frequency. A similar behavior was observed for other manganites [77–79], and different perovskite systems [80–82].

4 Conclusions

$\text{Pr}_{0.65}\text{Ca}_{0.25}\text{Cd}_{0.1}\text{MnO}_3$ ceramic was synthesized using a solid-state reaction method. Dc-conductivity analysis indicates that the studied ceramic exhibits a semiconductor behavior. Then, the hopping model governs the conduction mechanisms. From ac-measurements, the presence of the double exponent (s_1, s_2) is found. Such a result is attributed to the grain and grain boundary contribution. Two distinct conduction mechanisms are observed CBH, and OLPT ones. The analysis of the normalized imaginary part of impedance shows the presence of the relaxation process. Then, the analysis of the combined imaginary part of modulus and impedance confirms the presence of the relaxation process with non-Debye type. Dielectric

properties are characterized by the presence of a transition phase which can be related to the magnetic transition from ferromagnetic to paramagnetic behavior.

Compliance with ethical standards

Conflict of interest The authors declare that they have no conflict of interest.

References

1. X. Huang, L. Pei, Z. Liu, Z. Lu, Y. Sui, Z. Qian, W. Su, A study on PrMnO-based perovskite oxides used in SOFC cathodes. *J. Alloys Compd.* **365**, 265 (2002)
2. T. Ishihara, T. Kudo, H. Matsuda, Y. Takita, Doped PrMnO₃ perovskite oxide as a new cathode of solid oxide fuel cells for low temperature operation. *J. Electrochem. Soc.* **142**, 1519 (1995)
3. H.Y. Tu, Y. Takeda, N. Imanishi, O. Yamamoto, Ln_{0.4}Sr_{0.6}Co_{0.8}Fe_{0.2}O_{3-δ} (Ln = La, Pr, Nd, Sm, Gd) for the electrode in solid oxide fuel cells. *Solid State Ion.* **117**, 227 (1999)
4. GCh. Kostoglou, Ch. Ftikos, A. Ahmad-Khanlou, A. Naoumidis, D. Stover, Chemical compatibility of alternative perovskite oxide SOFC cathodes with doped lanthanum gallate solid electrolyte. *Solid State Ion.* **134**, 127 (2000)
5. H. Ullmann, N. Trofimenko, F. Tietz, D. Stover, A. Ahmad-Khanlou, Correlation between thermal expansion and oxide ion transport in mixed conducting perovskite-type oxides for SOFC cathodes. *Solid State Ion.* **138**, 79 (2000)
6. J. Hormes, M. Pantelouris, G.B. Balazs, B. Rambabu, X-ray absorption near edge structure (XANES) measurements of ceria-based solid electrolytes. *Solid State Ion.* **945**, 136 (2000)
7. A. Selmi, M. Khelifi, H. Rahmouni, R. M'nassri, K. Khirouni, N. Chniba Boudjada, A. Cheikhrouhou, Electrical conductivity analysis and magnetic properties of Pr_{0.7}Ca_{0.3}Mn_{0.95}Co_{0.05}O₃ oxide. *J. Mater. Sci. Mater. Electron.* **28**, 1901 (2017)
8. V.S. Kolat, H. Gencer, M. Gunes, S. Atalay, Effect of B-doping on the structural magnetotransport and magnetocaloric properties of La_{0.67}Ca_{0.33}MnO₃ compounds. *Mater. Sci. Eng. B* **140**, 212 (2007)
9. Z.C. Xia, S.L. Yuan, W. Feng, L.J. Zhang, G.H. Zang, J. Tang, L. Liu, D.W. Liu, Q.H. Zheng, L. Chen, Z.H. Fang, S. Liu, C.Q. Tang, Magnetoresistance and transport properties of different impurity doped La_{0.67}Ca_{0.33}MnO₃ composite. *Solid State Commun.* **127**, 572 (2003)
10. N. Khare, D.P. Singh, H.K. Gupta, P.K. Siwach, O.N. Srivastava, Preparation and study of silver added La_{0.67}Ca_{0.33}MnO₃ film. *J. Phys. Chem. Solids* **65**, 870 (2004)
11. T. Zhang, Y.Z. Fang, M. Dressel, X.P. Wang, Q.F. Fang, Nanometer size effect on the structure and magnetic properties of high oxygen content ferromagnetic PrMnO_{3+δ} nanoparticles. *J. Appl. Phys.* **108**, 113901 (2010)
12. N. Jiang, Y. Jiang, Q. Lu, S. Zhao, Dynamic exchange effect induced multi-state magnetic phase diagram in manganese oxide Pr_{1-x}Ca_xMnO₃. *J. Alloys Compd.* **805**, 50 (2019)
13. H. Rim, S. Jeung, E. Jung, J.S. Lee, Characteristics of Pr_{1-x}M_xMnO₃, (M = Ca, Sr) as cathode material in solid oxide fuel cells. *Mater. Chem. Phys.* **52**, 54 (1998)
14. A. Biswas, I. Das, C. Majumdar, Modification of the charge ordering in Pr_{1/2}Sr_{1/2}MnO₃ nanoparticles. *J. Appl. Phys.* **98**, 124310 (2005)
15. Z. Ur Rehman, M.S. Anwar, B. Koo, Influence of barium doping on the magnetic and magnetocaloric properties of Pr_{1-x}Ba_xMnO₃. *J. Super. Nov. Mag.* **28**, 1629 (2015)
16. P. Doggali, Y. Teraoka, S. Rayalu, N. Labhsetwa, Effect of A-site substitution in perovskites: catalytic properties of PrMnO₃ and Ba/K/Ce substituted PrMnO₃ for CO and PM oxidation. *J. Environ. Chem. Eng.* **3**, 420 (2015)
17. M. Khelifi, R. M'nassri, A. Selmi, H. Rahmouni, K. Khirouni, N. Chniba Boudjadad, A. Cheikhrouhou, Investigation of magnetic and transport properties of PrCa(MnCo)O prepared by solid state process. *J. Magn. Magn. Mater.* **423**, 20 (2017)
18. Z. Han, The low temperature specific heat and electrical transport, magnetic properties of Pr_{0.65}Ca_{0.35}MnO₃. *J. Magn. Magn. Mater.* **423**, 171 (2016)
19. R. Kondo, H. Okimura, Y. Sakai, Electrical properties of semiconductor photodiodes with semitransparent films. *Jpn. J. Appl. Phys.* **10**, 154 (1971)

20. F.A. Benko, F.P. Koffyberg, Quantum efficiency and optical transitions of CdO photo anodes. *Solid State Commun.* **57**, 90 (1986)
21. C. Sravani, K.T.R. Reddy, O.M. Hussain, P.J. Reddy, Investigations on n-CdO/p-CdTe thin film heterojunctions. *Thin Solid Films* **253**, 339 (1994)
22. L.M. Su, N. Grote, F. Schmitt, Diffused planar InP bipolar transistor with a cadmium oxide film emitter. *Electron. Lett.* **20**, 716 (1984)
23. A.S. Aldwayyan, F.M. Al-Jekhadab, M. Al-Noaimi, B. Hammouti, T.B. Hadda, M. Suleiman, I. Warad, Synthesis and characterization of CdO nanoparticles starting from organometallic Dmphen-CdI₂ complex. *Int. J. Electrochem. Sci.* **8**, 10506 (2013)
24. V. Gupta, B. Raina, K.K. Bamza, Preparation, structural, spectroscopic and magneto-electric properties of multiferroic cadmium doped neodmium manganite. *J. Mater. Sci. Mater. Electron.* **29**, 8947 (2018)
25. V. Gupta, B. Raina, S. Verma, K.K. Bamzai, Study of structural, spectroscopic and dielectric properties of multiferroic cadmium doped Samarium manganite synthesized by solid state reaction method. *AIP Conf. Proc.* **1953**, 050010 (2018)
26. J.P. Arauhjo, V.S. Amaral, P.B. Tavares, F. Lencart-Silva, A.A.C.S. Lourenço, E. Alves, J.B. Sousa, J.M. Vieira, Cadmium addition to vacancy doped lanthanum manganites: from metallic to insulator behaviour. *J. Magn. Magn. Mater.* **226**, 797 (2001)
27. I.O. Troyanchuk, D.D. Khalyavin, S.N. Pastushonok, Effect of Cd ions on transport properties of orthomanganites. *J. Phys. Condens. Matter* **10**, 185 (1998)
28. N.H. Luong, D.T. Hanh, N. Chau, N.D. Tho, T.D. Hiep, Properties of perovskites La_{1-x}Cd_xMnO₃. *J. Magn. Magn. Mater.* **290**, 690 (2005)
29. C. Saravanan, R. Thiyagarajan, K. Manikandan, M. Sathiskumar, P.V. Kanjariya, J.A. Bhalodia, S. Arumugam, Effect of Cd doping on magnetocaloric effect and critical behavior analysis on perovskite Nd_{1-x}Cd_xMnO₃ (x = 0, 0.1, 0.2, 0.3, and 0.4) manganite polycrystals. *J. Appl. Phys.* **122**, 245109 (2017)
30. P.V. Kanjariya, G.D. Jadav, C. Saravanan, L. Govindaraj, S. Arumugam, J.A. Bhalodia, Detailed investigations on structural properties and transport mechanism governed in Nd_{1-x}Cd_xMnO₃. *J. Mater. Sci. Mater. Electron.* **29**, 8107 (2018)
31. C. Saravanan, R. Thiyagarajan, P.V. Kanjariya, P. Sivaprakash, J.A. Bhalodia, S. Arumugam, Electrical resistivity, magnetic and magneto-caloric studies on perovskite manganites Nd_{1-x}Cd_xMnO₃ (x = 0 and 0.1) polycrystals. *J. Magn. Magn. Mater.* **476**, 35 (2019)
32. A. Pena, J. Gutiérrez, J.M. Barandiarra, J.P. Chapman, M. Insausti, T. Rojo, Correlation between structure and magnetic properties of Cd-substituted La_{0.7}(Ca_{0.3x}Cd_x)MnO₃ CMR manganite. *J. Solid State Chem.* **174**, 52 (2003)
33. H. Rahmouni, M. Smari, B. Cherif, E. Dhahrib, K. Khiroun, Conduction mechanism, impedance spectroscopic investigation and dielectric behavior of La_{0.5}Ca_{0.5-x}Ag_xMnO₃ manganites with compositions below the concentration limit of silver solubility in perovskites (0 ≤ x ≤ 0.2). *Dalton Trans.* **4**, 10457 (2015)
34. A. Bettaibi, R. M'nassri, A. Selmi, H. Rahmouni, N. Chniba-Boudjada, A. Chiekhrouhou, K. Khirouni, Effect of chromium concentration on the structural, magnetic and electrical properties of praseodymium-calcium manganite. *J. Alloys Compd.* **650**, 286 (2015)
35. N. Elghoul, M. Wali, S. Kraiem, H. Rahmouni, E. Dhahri, K. Khirouni, Sodium deficiency effect on the transport properties of La_{0.8}Na_{0.2-x}□_xMnO₃ manganites. *Phys. B Condes. Mater.* **478**, 108 (2015)
36. N.F. Mott, E.A. Davis, *Electronic Processes in Non-Crystalline Materials* (Oxford University Press, Oxford, 1979)
37. H.E. Sekrafi, A. Ben-JaziaKharrat, M.A. Wederni, K. Khirouni, N. Chniba-Boudjada, W. Boujelben, Structural, electrical, dielectric properties and conduction mechanism of sol-gel prepared Pr_{0.75}Bi_{0.05}Sr_{0.1}Ba_{0.1}Mn_{0.98}Ti_{0.02}O₃ compound. *Mater. Res. Bull.* **111**, 329 (2019)
38. A. Khlifi, A. Mleiki, H. Rahmouni, N. Guermazi, K. Khirouni, A. Cheikhrouhou, Barium deficiency and sintering temperature effects on structural and transport properties of La_{0.5}Eu_{0.2}Ba_{0.3-x}□_xMnO₃ manganite. *J. Mater. Sci. Mater. Electron.* **30**, 19513 (2019)
39. G.F. Pike, AC conductivity of scandium oxide and a new hopping model for conductivity. *Phys. Rev. B Solid State* **1572**, 6 (1972)
40. H. Rahmouni, B. Cherif, R. Jemai, A. Dhahri, K. Khirouni, Europium substitution for lanthanum in LaBaMnO. The structural and electrical properties of La_{0.7-x}Eu_xBa_{0.3}MnO₃ perovskite. *J. Alloys Compd.* **690**, 890 (2017)
41. A.K. Jonscher, New interpretation of dielectric loss peaks. *Nature* **253**, 717 (1975)
42. A.K. Jonscher, The 'universal' dielectric response. *Nature* **267**, 673 (1977)
43. K. Funke, Jump relaxation in solid electrolytes. *Prog. Solid State Chem.* **22**, 111 (1993)

44. S.R. Elliot, A.c. conduction in amorphous chalcogenide and pnictide semiconductors. *Adv. Phys.* **36**, 13 (1987)
45. A.B. Hassen, F.I.H. Rhouma, M. Daoudi, J. Dhahri, M. Zaidi, N. Abdelmoulae, Influence of defect on the electrical and optical properties of A-site non-stoichiometry $\text{Ca}_{0.67}\text{La}_{0.22}\text{Ti}_{(1-x)}\text{Cr}_x\text{O}_{3-8}$ perovskite. *RSC Adv.* **9**, 19285 (2019)
46. A. Satapathy, E. Sinha, B.K. Sonu, S.K. Rout, Conduction and relaxation phenomena in barium zirconate ceramic in wet N₂ environment. *J. Alloys Compd.* **811**, 152042 (2019)
47. A. Ben JaziaKharrat, S. Moussa, N. Moutiaa, K. Khirouni, W. Boujelben, Structural, electrical and dielectric properties of Bi-doped $\text{Pr}_{0.8-x}\text{Bi}_x\text{Sr}_{0.2}\text{MnO}_3$ manganite oxides prepared by sol–gel process. *J. Alloys Compd.* **724**, 389 (2017)
48. A.E. Neifeld, E.V. Arkhipov, A.N. Ugryumova, V.A. Korolyov, Y. Mukovsky, Temperature dependence of activation energy of the conductivity of manganites in paramagnetic phase. arXiv preprint [arXiv:cond-mat/0510362](https://arxiv.org/abs/cond-mat/0510362) (2005)
49. Y.B. Taher, A. Oueslati, N.K. Maaloul, K. Khirouni, M. Gargouri, Conductivity study and correlated barrier hopping (CBH) conduction mechanism in diphosphate compound. *Appl. Phys. A* **120**, 1537 (2015)
50. S. Amhil, L. Essaleh, S.M. Wasim, S.B. Moumen, G. Marin, A. Alimoussa, Overlapping large polaron tunneling conduction process in the ordered defect compound p-CuIn₃Se₅. *Mater. Res. Exp.* **5**, 085903 (2018)
51. B. Panda, K. Lokapriya Routray, D. Behera, Studies on conduction mechanism and dielectric properties of the nano-sized $\text{La}_{0.7}\text{Ca}_{0.3}\text{MnO}_3$ (LCMO) grains in the paramagnetic state. *Phys. B Condens. Matter* **583**, 411967 (2020)
52. J.L. García-Muñoz, C. Frontera, B. Rivas-Murias, J. Mira, Dielectric properties of $\text{Bi}_{1-x}\text{Sr}_x\text{MnO}_3$ ($x = 0.40, 0.50$) manganites: influence of room temperature charge order. *J. Appl. Phys.* **105**, 084116 (2009)
53. V. Khopkar, S. Balaram, Low temperature dielectric properties and NTCR behavior of $\text{BaFe}_{0.5}\text{Nb}_{0.5}\text{O}_3$ double perovskite ceramic. *Phys. Chem. Chem. Phys.* **22**, 2986 (2020)
54. I. Coondoo, N. Panwar, M. AsifRafiq, V.S. Puli, M. Nadeem Rafiq, R.S. Katiyar, Structural, dielectric and impedance spectroscopy studies in $(\text{Bi}_{1.0}\text{R}_{0.10})\text{Fe}_{0.95}\text{Sc}_{0.05}\text{O}_3$ [$\text{R} = \text{La}, \text{Nd}$] ceramics. *Ceram. Int.* **40**, 9895 (2014)
55. M. Sassi, A. Bettaibi, A. Oueslati, K. Khirouni, M. Gargouri, Electrical conduction mechanism and transport properties of LiCrP_2O_7 compound. *J. Alloys Compd.* **649**, 642 (2015)
56. S. Mathlouthi, A. Oueslati, B. Louati, AC conductivity and conduction mechanism study of rubidium gadolinium diphosphate compound. *Ind. J. Phys.* **93**, 603 (2019)
57. R. Martinez, A. Kumar, R. Palai, J.F. Scott, R.S. Katiyar, Impedance spectroscopy analysis of $\text{Ba}_{0.7}\text{Sr}_{0.3}\text{TiO}_3/\text{La}_{0.7}\text{Sr}_{0.3}\text{MnO}_3$ heterostructure. *J. Phys. D Appl. Phys.* **44**, 105302 (2011)
58. R.N. Bhowmik, A.G. Lone, Dielectric properties of $\alpha\text{-Fe}_{1.6}\text{Ga}_{0.4}\text{O}_3$ oxide: a promising magneto-electric material. *J. Alloys Compd.* **680**, 31 (2016)
59. N. Assoudi, W. Hzez, R. Dhahri, I. Walha, H. Rahmouni, K. Khirouni, E. Dhahri, Physical properties of Ag/Ca doped Lanthanum manganite. *J. Mater. Sci. Mater. Electron.* **29**, 20113 (2018)
60. M. Nadeem, M.J. Akhtar, Melting/collapse of charge orbital ordering and spread of relaxation time with frequency in $\text{La}_{0.5}\text{Ca}_{0.5}\text{MnO}_{3+y}$ by impedance spectroscopy. *J. Appl. Phys.* **104**, 103713 (2008)
61. R. Ranjan, R. Kumar, N. Kumar, B. Behera, R.N.P. Choudhary, Impedance and electric modulus analysis of Sm-modified $\text{Pb}(\text{Zr}_{0.55}\text{Ti}_{0.45})_{1-x/4}\text{O}_3$ ceramics. *J. Alloys Compd.* **509**, 6394 (2011)
62. R. Chargaia, S. Hcini, M. Boudard, A. Dhahri, Microstructural properties, conduction mechanism, dielectric behavior, impedance and electrical modulus of $\text{La}_{0.6}\text{Sr}_{0.2}\text{Na}_{0.2}\text{MnO}_3$ manganite. *J. Mater. Sci. Mater. Electron.* **30**(3), 2975 (2019)
63. M. Idrees, M. Nadeem, M.M. Hassan, Investigation of conduction and relaxation phenomena in $\text{LaFe}_{0.9}\text{Ni}_{0.1}\text{O}_3$ by impedance spectroscopy. *J. Phys. D.* **43**, 155401 (2010)
64. I. Ahmad, M.J. Akhtar, R.T.A. Khan, M.M. Hasan, Change of Mott variable range to small polaronic hole hopping conduction mechanism and formation of Schottky barriers in $\text{Nd}_{0.9}\text{Sr}_{0.1}\text{FeO}_3$. *J. Appl. Phys.* **114**, 034103 (2013)
65. W. Bai, G. Chen, J.Y. Zhu, J. Yangand, T. Lin, Dielectric responses and scaling behaviors in Aurivillius $\text{Bi}_6\text{Ti}_3\text{Fe}_2\text{O}_{18}$ multiferroic thin films. *Appl. Phys. Lett.* **100**, 082902 (2012)
66. Q. Ke, X. Lou, Y. Wang, J. Wang, Oxygen-vacancy-related relaxation and scaling behaviors of $\text{Bi}_{0.9}\text{La}_{0.1}\text{Fe}_{0.98}\text{Mg}_{0.02}\text{O}_3$ ferroelectric thin film. *Phys. Rev. B Condens. Matter Mater. Phys.* **82**, 024102 (2010)
67. A.E. Stearn, H. Hyring, The deduction of reaction mechanisms from the theory of absolute rates. *J. Chem. Phys.* **5**, 113 (1937)
68. S. Thakura, R. Raia, I. Bdikinb, M. Almeida Valente, Impedance and modulus spectroscopy characterization of Tb modified $\text{Bi}_{0.8}\text{A}_{0.1}\text{Pb}_{0.1}\text{Fe}_{0.9}\text{Ti}_{0.1}\text{O}_3$ ceramics. *Mater. Res.* **19**, 1 (2016)

69. N.V. Prasad, G.V. Prasad, T. Bhimasankaram, G.S. Kumar Suryanarayana, Synthesis, impedance and dielectric properties of $\text{LaBi}_5\text{Fe}_2\text{Ti}_3\text{O}_{18}$. *Bull. Mater. Sci.* **24**, 487 (2001)
70. G. Ranga Mohan, D. Ravinder, A.V. Ramana Reddy, B.S. Boyanov, Dielectric properties of polycrystalline mixed nickel–zinc ferrites. *Mater. Lett.* **40**, 39 (1999)
71. J.C. Anderson, *Dielectrics* (Chapman & Hall, London, 1964)
72. R. Lahouli, J. Massoudi, M. Smari, H. Rahmouni, K. Khirouni, E. Dhahri, L. Bessais, Investigation of annealing effects on the physical properties of $\text{Ni}_{0.6}\text{Zn}_{0.4}\text{Fe}_{1.5}\text{Al}_{0.5}\text{O}_4$ ferrite. *RSC Adv.* **9**, 19949 (2019)
73. T. Kar, R.N.P. Choudhary, Structural dielectric and electrical properties of LiNbMoO_6 ceramics. *Mater. Lett.* **32**, 109 (1997)
74. T. Kar, R.N.P. Choudhary, Structural, dielectric and electrical conducting properties of CsBBO_6 (B = Nb, Ta; B = W, Mo) ceramics. *Mater. Sci. Eng.* **90**, 224 (2002)
75. T. Kar, Structural and dielectric properties of defect pyrochlore-type ABWO_6 ceramic. *Pramana Res. J.* **9**, 2249 (2019)
76. H.M. Rai, S.K. Saxena, R. Late, V. Mishra, P. Rajput, A. Sagdeo, R. Kumara, P.R. Sagdeo, Observation of large dielectric permittivity and dielectric relaxation phenomenon in Mn-doped lanthanum gallate. *RSC Adv.* **6**, 2662 (2016)
77. R.S. Freitas, J.F. Mitchell, P. Schiffer, Magnetodielectric consequences of phase separation in the colossal magnetoresistance manganite $\text{Pr}_{0.7}\text{Ca}_{0.3}\text{MnO}_3$. *Phys. Rev. B Condens. Matter Mater.* **72**, 144429 (2005)
78. J.L. Cohn, M. Peterca, J.J. Neumeier, Low-temperature permittivity of insulating perovskite manganites. *Phys. Rev B* **70**, 214433 (2004)
79. J.L. Cohn, M. Peterca, J.J. Neumeier, Giant dielectric permittivity of electron-doped manganite thin films, $\text{Ca}_{1-x}\text{La}_x\text{MnO}_3$ ($0 \leq x \leq 0.03$). *J. Appl. Phys.* **97**, 034102 (2005)
80. V.G. Nair, A. Das, V. Subramanian, P.N. Santhosh, Magnetic structure and magnetodielectric effect of $\text{YFe}_{0.5}\text{Cr}_{0.5}\text{O}_3$. *J. Appl. Phys.* **113**, 213907 (2013)
81. V.G. Nair, L. Pal, V. Subramanian, P.N. Santhosh, Structural, magnetic, and magnetodielectric studies of metamagnetic $\text{DyFe}_{0.5}\text{Cr}_{0.5}\text{O}_3$. *J. Appl. Phys.* **115**, 17D728 (2014)
82. O. Bidault, M. Maglione, M. Actis, M. Kchikech, B. Salce, Polaronic relaxation in perovskites. *Phys. Rev. B Condens. Matter Mater.* **52**, 4191 (1995)